



New fast integrated mobility spectrometer for real-time measurement of aerosol size distribution: II. Design, calibration, and performance characterization[☆]

Pramod Kulkarni, Jian Wang*

Brookhaven National Laboratory, Building 815E, Upton, NY 11973-5000, USA

Received 15 November 2005; received in revised form 6 January 2006; accepted 17 January 2006

Abstract

A Fast Integrated Mobility Spectrometer (FIMS) has been developed for sub-second aerosol size distribution measurements based on the description presented in the preceding paper (Paper I). The performance of FIMS was characterized using DMA classified aerosols in the size range 15–170 nm. An excellent agreement was observed between the mean particle diameter measured by FIMS and the DMA centroid diameter. Comparison of particle concentrations measured by FIMS and a Condensation Particle Counter (CPC) shows that counting efficiency of FIMS is 100% for particles larger than 20 nm, and higher than that of the CPC for particles with diameters less than 15 nm. Experimentally determined FIMS mobility resolution ranged from 5 to 14 for particle diameters between 22 to 170 nm, and agreed with theoretical predictions made using FIMS transfer theory, though there was some deviation observed at particle sizes that correspond to high theoretical mobility resolution.

© 2006 Elsevier Ltd. All rights reserved.

Keywords: Aerosol size distribution measurements; High time resolution; Electric mobility; Transfer function; Counting efficiency; Particle diffusion; Mobility resolution

1. Introduction

A Fast Integrated Mobility Spectrometer (FIMS) for real-time measurement of sub-micrometer aerosol size distributions (15–1000 nm) has been developed based on the description presented in the preceding paper (Paper I). The FIMS first separates aerosol particles based on their electrical mobility in a uniform electric field generated by a parallel plate geometry, and subsequently grows them into super-micrometer droplets in a supersaturation environment. The detector—a high speed camera—records the mobility-dependent particle positions and counts, which are then used to derive particle electrical mobility and concentration. By detecting particle of different sizes simultaneously, the FIMS eliminates the need for voltage scanning required in traditional scanning mobility techniques, and ensures

[☆] This manuscript has been authored by Brookhaven Science Associates, LLC under Contract No. DE-AC02-98CH1-886 with the U.S. Department of Energy. The United States Government retains, and the publisher, by accepting the article for publication, acknowledges, a world-wide license to publish or reproduce the published form of this manuscript, or allow others to do so, for the United States Government purposes.

* Corresponding author. Tel.: +1 631 344 7920; fax: +1 631 344 2887.

E-mail address: jian@bnl.gov (J. Wang).

significant increases in both measurement speed and counting statistics. This paper describes design and performance characterization of a prototype FIMS based on the analysis presented in Paper I.

Standard calibration techniques, pertinent to characterization of FIMS, are briefly reviewed below. Although there are many methods, the cylindrical DMA has been extensively used to generate monodisperse aerosols for instrument calibrations. Agarwal and Sem (1978) described calibration of a DMA using monodisperse particles that were classified from a polydisperse aerosol with a second DMA. In their method, two DMAs are used in a sequence such that the ‘quasi-monodisperse’ aerosol from the first DMA is input to the second DMA for calibration. This method, which is often referred to as Tandem DMA (TDMA) technique (Rader & McMurry, 1986), has been extensively used to determine the DMA transfer function and to study the broadening of the transfer function due to Brownian diffusion of small particles. Kousaka, Okuyama, Adachi, and Mimura (1986) investigated, both theoretically and experimentally, the diffusional broadening of DMA transfer function. Stolzenburg (1988) performed detailed analysis of particle Brownian diffusion in a cylindrical DMA and derived an analytical expression for DMA transfer function that accounts for both migration and Brownian diffusion. He showed that the diffusional broadening of the DMA transfer function is characterized by a spread factor (σ) that represents non-dimensional variance in the particle stream function. He also experimentally measured the spread factor using the TDMA method and showed that the measured spread factor agreed with the theoretical value at aerosol to sheath flow ratio (β) of 0.1, but was slightly higher than the predicted value at $\beta = 0.05$. Zhang and Flagan (1996) extended the Stolzenburg’s model to derive the transfer function of their radial DMA. They also measured the spread factor using TDMA technique, and found the measured σ was higher than the theoretical prediction. Zhang and Flagan (1996) concluded that the discrepancy was possibly due to non-idealities in flow and electrical fields inside the radial DMA.

Following the convention in spectroscopic literature, Zhang and Flagan (1996) proposed that the performance of DMAs could be characterized in terms of mobility resolution, which is defined as the ratio of the mobility at the peak of the transfer function to the full width at half the peak height of transfer function. Thus, mobility resolution characterizes the relative uncertainty in measured mobility. Their experimental results showed that the resolution of radial DMA approached the theoretical limit at small Peclet numbers, but fell below the theoretical value in the large Peclet number limit, suggesting that the cause for this deviation could be attributed to the flow distortion at the aerosol entrance. Stolzenburg’s (1988) study of cylindrical DMA also showed similar deviation, though smaller in magnitude, at high flow rates—possibly resulting from entrance flow arrangement.

In this paper, we report detailed calibration and characterization of a prototype FIMS. Using a technique similar to TDMA, the diffusion broadening of the FIMS transfer function has been characterized by operating a cylindrical DMA and FIMS in series. The response of FIMS to the monodisperse aerosol classified by the DMA can be theoretically predicted using the FIMS transfer function derived in Paper I. The spread factor (σ) in the FIMS transfer function was derived by fitting the theoretical model to measured FIMS response. The derived spread factor and the FIMS resolution calculated using the experimentally derived σ are compared to theoretical values, and the possible reasons for observed discrepancies are discussed.

2. Experimental

2.1. Instrument design

The schematic cross section of FIMS is shown in Fig. 1. The design of the prototype was based on analyses presented in Paper I. The entire parallel plate geometry is divided into four detachable sections—(i) entrance, (ii) separator, (iii) condenser, and (iv) detector, and were designed such that when all sections are put together in a sequence, a rectangular channel with a clear cross-sectional area of 1 cm \times 10 cm is formed in x - z plane. Individual section can be disassembled for maintenance purposes without losing mechanical precision. The key physical dimensions of the prototype FIMS are same as those of Units 2–4 presented in Paper I. Particle-free sheath air, saturated with *n*-butanol enters the channel through ports located at the top of entrance section. The sheath flow then passes through a fine screen that evenly distributes the flow, and provides a uniform flow field at the entrance. The aerosol flow enters the main channel tangentially through a 1 mm wide slit. The slit spans over the entire width of 10 cm in the z -direction. Length of the entrance section is maintained sufficiently long to ensure a fully developed sheath flow at the aerosol entrance. The two embedded steel plate-electrodes create a uniform electric field in the flow passage and are insulated from the rest of the

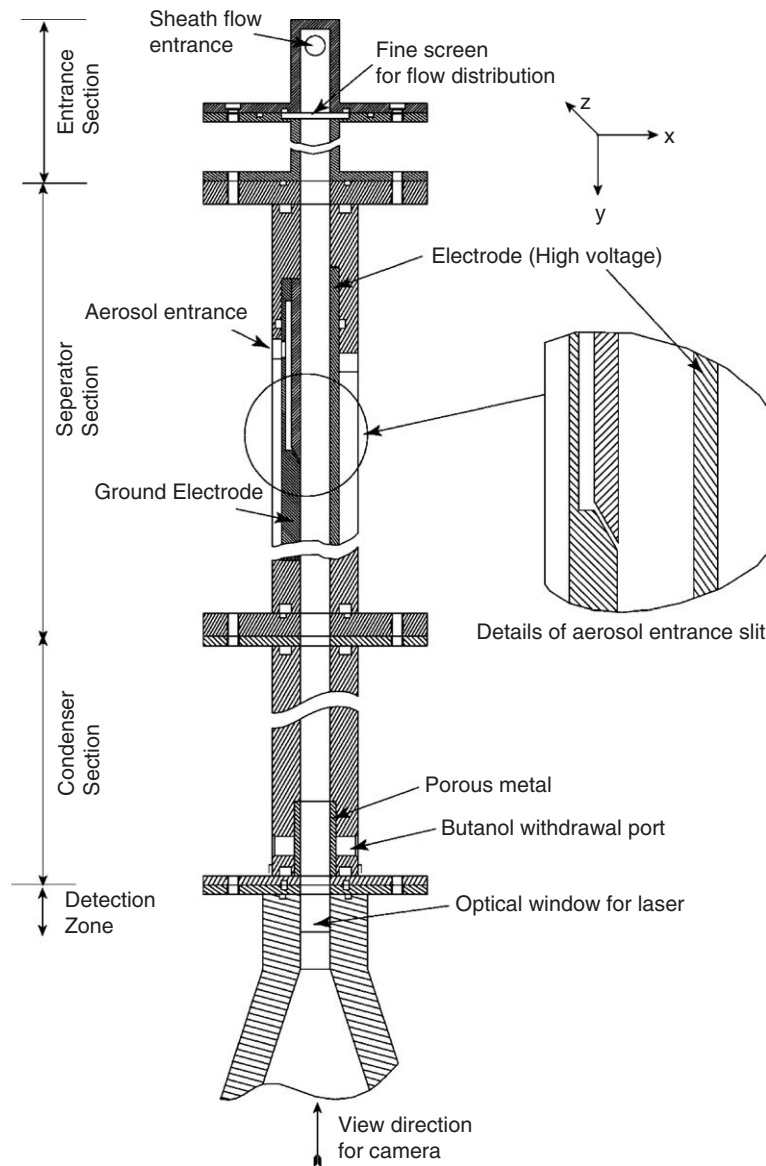


Fig. 1. Schematic diagram of the prototype Fast Integrated Mobility Spectrometer.

separator body. The distance between the electrodes in the x -direction (a) is 1 cm, and their effective length from aerosol entrance slit to the end of electrode is 20 cm (l_s). The width of electrodes in the z -direction (b) is 10 cm. The electrode with an aerosol entrance slit (left electrode) is grounded, and a negative potential is applied to the other (right) electrode. The electrodes in the separator are insulated from the body of the condenser using 2 cm long (along y -direction) plastic plates. This effectively reduces the electric field strength at the electrode edges to levels below the corona initiation strength. The walls of the condenser are made of aluminum, and are cooled to 5 °C using thermoelectric coolers mounted on the outside walls. The condenser is thermally insulated from the ambient air using Neoprene pads. The end zone of the condenser is provided with inner porous walls. Butanol condensed on the inner surfaces is constantly withdrawn through the porous walls using a peristaltic pump, which prevents accumulation of butanol. The effective length of condenser (l_c) is 30 cm. Optical windows are provided in the detection zone, and are seated in the walls with their inside surfaces flush with the channel surfaces to allow unobstructed airflow. These windows allow laser light to pass through and illuminate aerosol particles traveling across x - z plane in the channel. The sheath air, after passing through

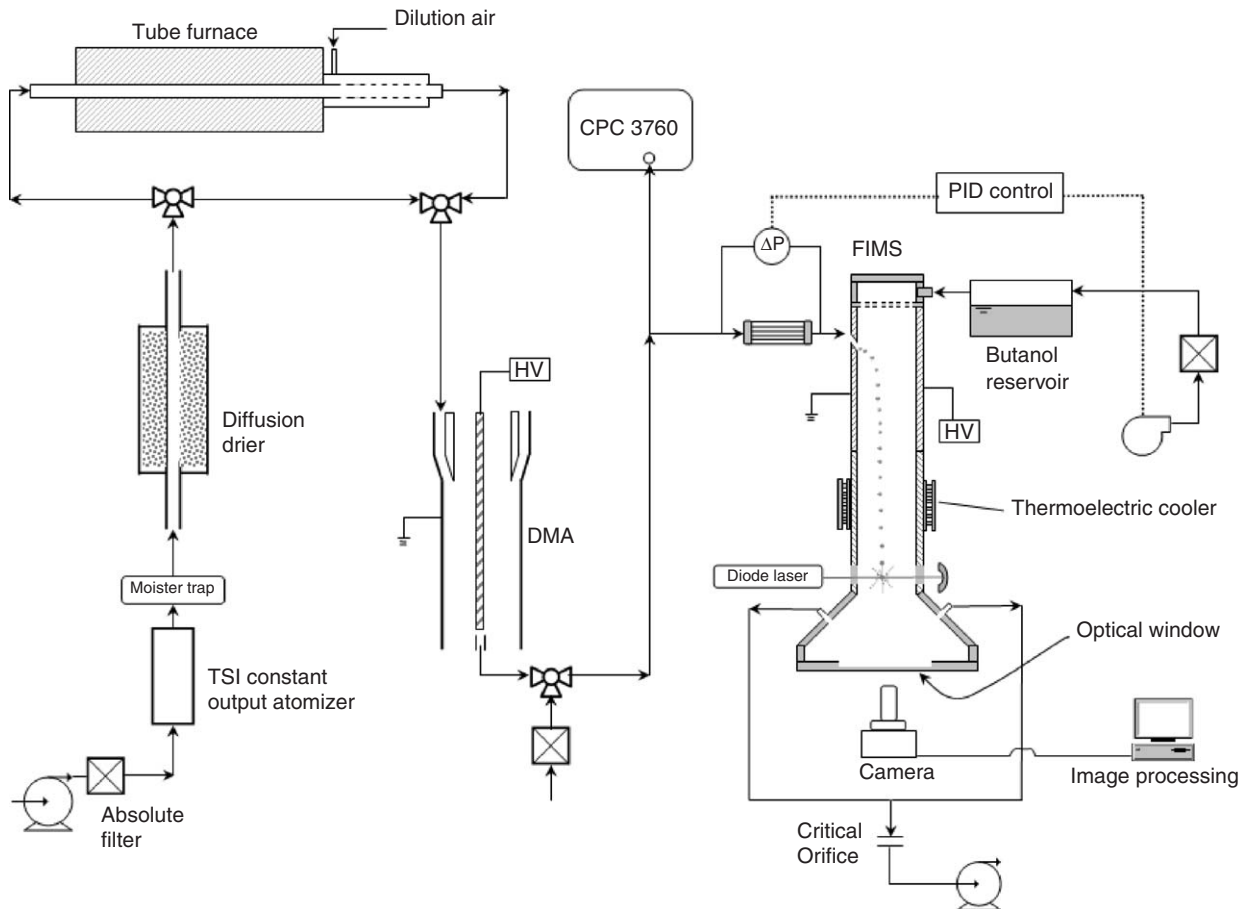


Fig. 2. Experimental setup for characterizing the prototype FIMS.

the detection zone, exits through a diverging section and is exhausted using a vacuum pump. Another optical window (in x - z plane) is provided at the end of diverging section that allows viewing of illuminated particles in the detection zone. The entire geometry was designed to allow an unobstructed air flow from the sheath flow inlet to the detection zone.

The detection system consists of a laser, lenses, and a Charge-Coupled Device (CCD) camera. The elliptical beam from the diode laser ($\lambda = 532$ nm CW, 50 mW; Brimrose Corp.) is collimated to a thin sheet with a width of 1 cm (in x -direction) and height of 1 mm (in y -direction) using a combination of concave and convex lenses. The laser light ensures illumination of all particles traveling across x - z plane between the two electrodes. The scattered light from the particles is detected by the high speed CCD camera (DALSA 1M60, Dalsa Corp., Germany) viewing the x - z plane in the detection region from a negative y -direction. The CCD sensor has a resolution of 1024×1024 , pixel size of $12 \mu\text{m} \times 12 \mu\text{m}$, and can be operated at a rate up to 60 frames per second. A camera lens is used to image the particles onto the CCD sensor with a magnification ratio of ~ 0.22 . The camera is controlled by a computer through a frame grabber (NI PCI-1428, National Instruments) that uses a camera link interface for high speed image acquisition. Images recorded by the camera are used to retrieve the counts and positions of particles in the x - z plane, and are saved for post-processing.

2.2. Experimental setup

Experimental setup used for characterization of the FIMS is shown in Fig. 2. The instrument was characterized using monodisperse $(\text{NH}_4)_2\text{SO}_4$ and NaCl aerosols classified by a cylindrical DMA (TSI Inc. Model 3081). NaCl aerosols were generated in the size range from 12 to 47 nm by atomizing a dilute NaCl (40 mM) solution using a constant output

atomizer (TSI Inc., Model 3076), followed by an evaporation–condensation growth in a tube furnace and subsequent diffusion drying. The output particle size distribution was controlled by varying the flow rate of the dilution or quench air flow at the furnace outlet and optimizing the furnace temperature between 500 to 700 °C. For the larger size range (50–170 nm), $(\text{NH}_4)_2\text{SO}_4$ aerosols were generated by atomizing dilute $(\text{NH}_4)_2\text{SO}_4$ solution, followed by diffusion drying. The concentration of the $(\text{NH}_4)_2\text{SO}_4$ solution in the atomizer was optimized to achieve the desired particle size range. The polydisperse aerosols generated by either of these two methods were subsequently classified in the DMA to obtain monodisperse aerosol with desired size. The aerosol and sample flows of the DMA were maintained at 1 lpm and the sheath and excess flows were controlled at 10 lpm. The classified, monodisperse aerosol was then split into two flows, one directed to a condensation particle counter (CPC; TSI Inc. Model 3760A), and the other to the aerosol inlet of FIMS. The aerosol flow rate of FIMS was monitored using a laminar flow element and a differential pressure transducer, located just upstream of the aerosol inlet.

A vacuum pump along with a critical orifice was used to maintain a constant total flow (Q_t) through FIMS. Sheath flow was supplied using a blower that was operated using a PID controller to achieve the desired aerosol flow (Q_a). Before entering the FIMS, the particle-free sheath flow passed through a butanol reservoir, where it was saturated with butanol. The temperature of the reservoir was kept at 25 °C. The walls of the condenser were maintained at 5 °C using a PID controller (Wavelength Electronics, MPI 10 000) with a feedback loop from thermistors mounted on the outer walls of the condenser. All flows were calibrated with a flow calibrator (Gilibrator, Gilian Instruments), and the variability of the sheath flow was estimated at 1%. All the data and image acquisition was performed using LabVIEW (National Instruments). The pictures recorded by the camera were 8-bit, grayscale images that were further processed using NI Vision software (National Instruments) to obtain particle position and counts. In order to avoid flow edge effects, only particles that appeared in the central region spanning 5.6 cm (in z -direction) were included in data analysis. To obtain the position of each particle, each image was converted to a binary image using a threshold pixel value that clearly differentiated the particle images from the background. The center of the converted binary particle image was then computed, and taken as the particle location in x – z plane.

Before starting each experiment, the aerosol generation system was allowed to stabilize. The temperatures of the butanol reservoir and the FIMS condenser were also allowed to reach equilibrium.

3. Results and discussion

3.1. Size measurement with DMA classified aerosol

The first step in processing images acquired by the CCD camera involves computing particle positions, particularly their x -coordinates, and the total particle counts in each image. The narrow mobility distribution of the monodisperse aerosol classified by the DMA, combined with the finite mobility resolution of the FIMS, leads to a distribution of the particle x -coordinates at the exit of the condenser. Once the locations of all particles are derived from the recorded images, this distribution can be obtained by binning the distance between the electrodes into, say, 50 bins, and then counting the number of particles whose x -coordinates fall into the respective bins.

Fig. 3 shows such coordinate distributions for a DMA classified 53 nm $(\text{NH}_4)_2\text{SO}_4$ aerosol at four different voltages ranging from 0 to 525 V. As no aerosol neutralizer was used between the DMA outlet and the inlet of FIMS, particles entering the FIMS were all charged. The y -axis in Fig. 3 represents number concentration, normalized by the peak concentration, and x -axis shows x -coordinates of particles from the images. $x = 0$ corresponds to the left electrode (ground electrode), and the right electrode is located at $x = 10$ mm. Distributions are averaged using data from about 300 images acquired over 5 s. As expected, the particle position distribution at the condenser exit is close to the left electrode when no voltage is applied in the separator (i.e. $V = 0$). This distribution should be similar to that of uncharged particles when electric field is present, since particles do not experience any electrostatic force in both cases. The measured coordinate distribution at $V = 0$ is consistent with the particle transport simulations in Paper I, and ensures that there is no interference from the uncharged particles.

As the potential on the right electrode is increased from 0 to 125 V, the distribution shifts to the right due to the additional electrophoretic velocity in the x -direction. Fig. 3 shows that the distance traveled by particles increases with increasing separator voltage, which clearly demonstrates the feasibility of the principle employed by the FIMS. Though distributions reported in Fig. 3 were averaged over 5 s (using 300 frames, at a frame rate of 60 Hz), particle size distributions can also be obtained at much higher frequencies, up to a frame rate of the CCD camera (60 Hz). However

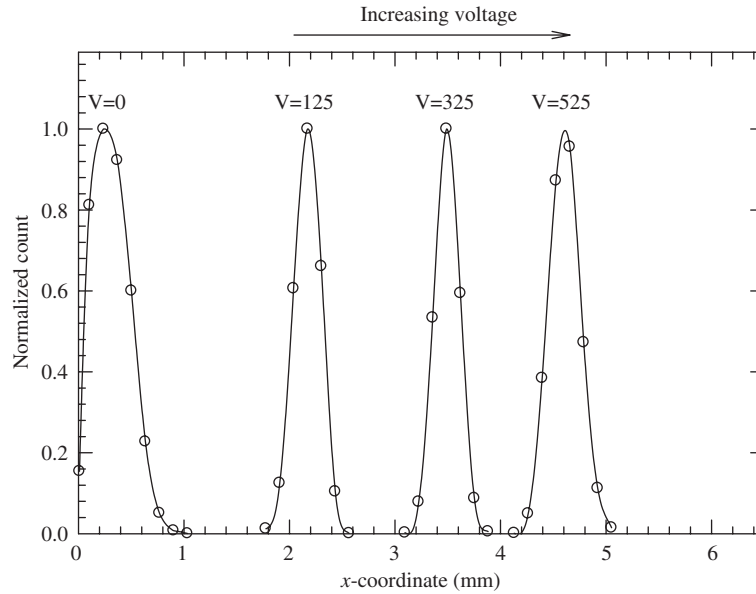


Fig. 3. Distribution of the x -coordinates recorded by the imaging system for a DMA classified, charged 53 nm $(\text{NH}_4)_2\text{SO}_4$ aerosol at different separator voltages. Particles are positively charged, and negative potential was applied on the right electrode. The distribution shifts to the right with increasing potential on the right electrode.

such high time resolution distributions are acceptable only if the associated counting statistics are satisfactory, as discussed in Paper I. In this paper, all distributions reported correspond to 5 s average of FIMS measurements.

Once the coordinate distribution for an aerosol is known, it can be converted to a distribution of the instrument response mobility. As shown in Paper I, the instrument response mobility can be calculated from the particle position \tilde{x} by

$$\frac{Z_p^*}{Z_{p_{\max}}^*} = \frac{2(1 + \beta)(3\tilde{x}^2 - 2\tilde{x}^3) - \beta}{2 + \beta}, \tag{1}$$

where β is the ratio of aerosol flow to sheath flow ($=Q_a/Q_{sh}$), and \tilde{x} the normalized particle x -coordinate derived from images. $Z_{p_{\max}}^*$ is the maximum mobility corresponding to minimum diameter measurable in FIMS, and can be calculated using the following equation

$$Z_{p_{\max}}^* \cong \frac{aQ_a}{\beta b l_s V}. \tag{2}$$

The sizing accuracy of FIMS was characterized using the DMA classified, monodisperse aerosols in the diameter range from 15 to 170 nm. Monodisperse aerosol with desired size is first obtained from the DMA, and then sent directly to FIMS without neutralizing. Experiments were carried out at two total flow rates of 9.7 and 11.85 lpm through FIMS. The ratio of aerosol flow to the sheath flow in FIMS, i.e. β , was maintained at 0.02 in all experiments. As discussed in Paper I, four FIMS units are required to cover the sub-micrometer size range from 5 to 1000 nm. Since the physical dimensions of FIMS are same for Units 2 and 3, the prototype FIMS can be used to characterize the performance of both units by operating at different separator voltages. The measurement range of Units 2 and 3 are 15–47 nm and 48–170 nm, respectively. The operating parameters for both units at two different total flow rates are listed in Table 1.

Images captured by the CCD camera at $Q_t = 9.7$ lpm are presented in Fig. 4. Images in Fig. 4(a), (b), (c), and (d) show locations of grown droplets corresponding to DMA centroid diameters of 24, 22, 170, and 120 nm, respectively. The droplet positions were then converted to instrument response mobility Z_p^* using Eqs. (1) and (2). Fig. 4(e) gives the response mobility distributions of the 22 and 24 nm particles measured by FIMS, and Fig. 4(f) shows the distributions for 120 and 170 nm particles. Assuming particles carried only one charge, the instrument response mobility Z_p^* was

Table 1

Operating conditions used in FIMS Units 2 and 3, which measure particles ranging from 15 to 170 nm

	Measurement range (nm)	Voltage (V)	
		$Q_t = 9.7$ lpm $Q_a = 0.19$ lpm	$Q_t = 11.85$ lpm $Q_a = 0.23$ lpm
Unit 2	15–47	73	90
Unit 3	47–170	750	916

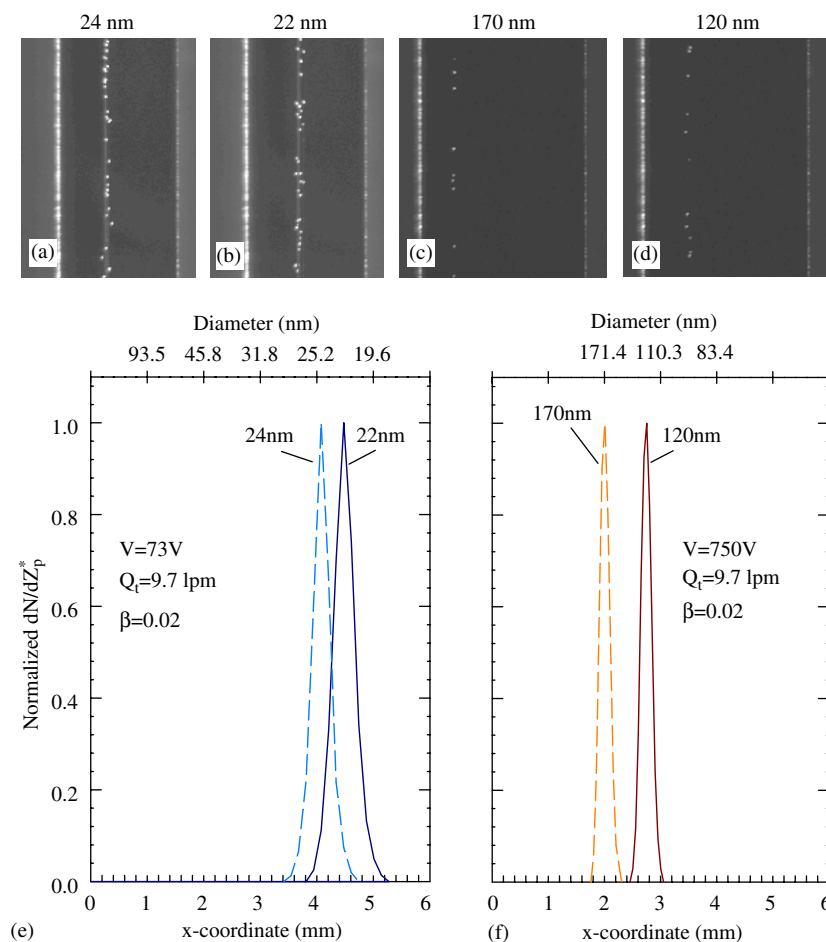


Fig. 4. Images obtained from the CCD (operating at 60 Hz) showing locations of: (a) 24 nm; (b) 22 nm NaCl particles in Unit 2; and (c) 170 nm; (d) 120 nm (NH₄)₂SO₄ particles in Unit 3. The corresponding response mobility distributions of particles detected are shown for (e) 22 and 24 nm; and (f) 120 and 170 nm.

also converted to particles diameters, which is shown on the top x-axes of Fig. 4(e)–(f). The peaks of distributions in Fig. 4(e) occur at 21.6 and 24.5 nm, and at 169.6 and 119.5 nm in Fig. 4(f), respectively.

The mean diameter of such distributions obtained from FIMS can then be compared with the DMA centroid diameter to assess the sizing accuracy of FIMS measurements. Fig. 5(a) and (b) show comparison of DMA centroid diameter to mean particle diameter from FIMS operated at $Q_t = 9.7$ and 11.85 lpm, respectively. The mean diameters in Fig. 5(a)–(b) were averaged over 6 to 10 runs, with each run having a sampling interval of 5 s. Error bars represent the standard deviation over the number of replicates used. Fig. 5(a) shows that mean particle diameters measured by FIMS agree very well with the DMA centroid diameter over the entire size range studied. At a total flow rate (Q_t) of 9.7 lpm,

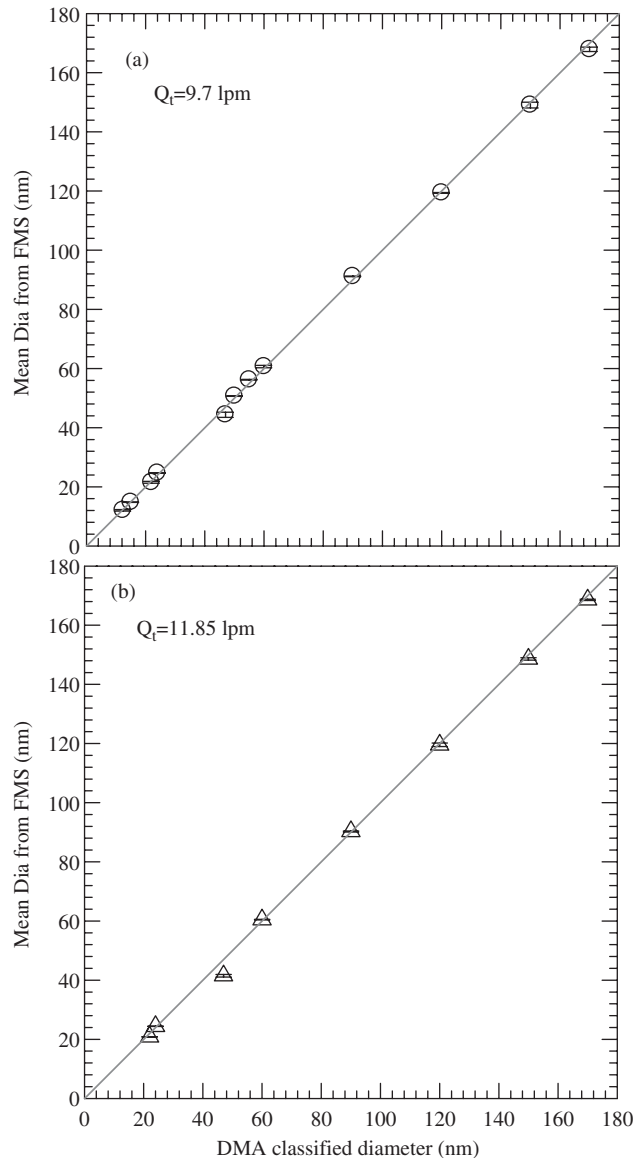


Fig. 5. Comparison of DMA centroid diameter and the mean diameter measured by FIMS over the diameter range of 12.3–170 nm at: (a) $Q_t = 9.7$ lpm; and (b) $Q_t = 11.85$ lpm.

the maximum deviation of the mean measured diameter from the DMA centroid diameter was 2.7% for 24 nm particles, and at $Q_t = 11.85$ lpm the maximum deviation was 5.3% for 50 nm particles. The maximum relative standard deviation was 0.68% at 60 nm for $Q_t = 9.7$ lpm, and 0.5% at 120 nm for $Q_t = 11.85$ lpm. These measurements demonstrate that the particle diameters can be measured by FIMS with high accuracy.

3.2. Counting efficiency of FIMS

The counting efficiency of FIMS was evaluated by comparing the total particle concentrations (N_{FIMS}) measured by the FIMS to those simultaneously measured by the CPC (N_{CPC}) over a wide range of particle diameters. As discussed in Paper I, the counting efficiency mainly depends on the particle size dependent activation efficiency, which is controlled by the local saturation ratio along the particle trajectory in the condenser. Counting efficiency also depends on whether

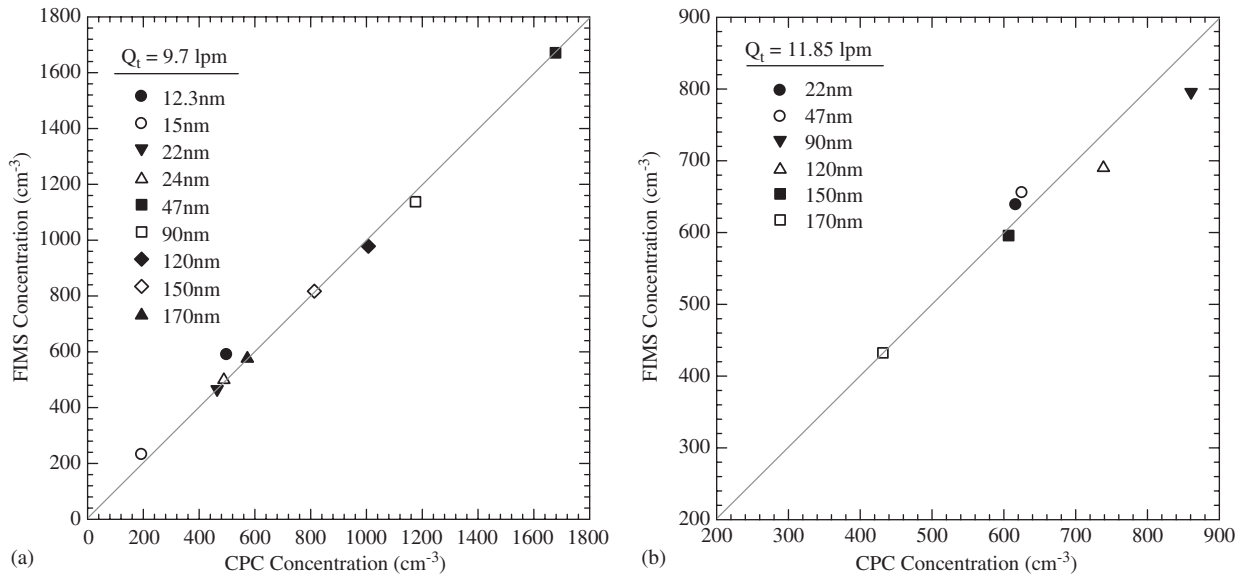


Fig. 6. Comparison of particle number concentration recorded by CPC to that measured by FIMS at: (a) $Q_t = 9.7$ lpm; and (b) $Q_t = 11.85$ lpm.

the particles can grow to optically detectable droplets. Detailed particle transport and growth simulations were presented in Paper I, which showed particles as small as 5 nm in diameter can be activated and grown into droplets larger than 120 μm .

Once the total particle count from each frame is known, the number concentration of aerosol sample can be calculated using the following equation

$$N_{\text{FIMS}} = \frac{n_{\text{fps}} \cdot C_{\text{frame}}}{(Q_a A_{\text{view}}/ab)}, \quad (3)$$

where C_{frame} is the number of particle counts in a frame, n_{fps} is the frame speed, and A_{view} is the area of the view region in x - z plane (equal to 1 cm \times 5.6 cm in this work), over which particle counting was performed. Consistent with the definition in Paper I, the aerosol flow Q_a used in the above equation is the effective flow rate corresponding to two-dimensional flow extended to the full width of the channel (10 cm).

Fig. 6(a) and (b) show comparison of concentrations measured by FIMS and the CPC. The CPC (TSI Inc. Model 3760A) has a 50% counting efficiency at 11 nm. As seen in the figure, for particles larger than 20 nm, the concentrations measured by FIMS agree very well with those measured by the CPC, suggesting the particle losses within FIMS are negligible and the counting efficiency is 100%. At $Q_t = 9.7$ lpm, concentration of 12.3 and 15 nm particles measured by FIMS were 15.4% and 16.5% higher than those measured by the CPC, respectively, indicating better FIMS counting efficiencies at small particle sizes. Similarly, at $Q_t = 11.85$ lpm, the FIMS concentrations are 34.6% and 46.1% higher than the CPC concentrations for 12.3 and 15 nm particles, respectively. Detailed characterization of the counting efficiency and particle losses inside the FIMS at various temperatures and flow rates will provide a better quantification of the FIMS performance, and will be a subject of future studies.

3.3. Diffusional spreading of small particles

As discussed in Paper I, Brownian diffusion of small particles can substantially decrease the mobility resolution of FIMS. Paper I presents an analytical FIMS transfer function in which the particle diffusion is characterized by a non-dimensional spread factor σ (Eq. (43) in Paper I). The transfer function can be used to independently predict the responses of FIMS to known aerosol size distributions. On the other hand, by fitting the theoretical prediction to the measured instrument response to monodisperse aerosols, the spread factor σ can be derived. Let $n_1(Z_p)$ represent the mobility distribution of the polydisperse aerosol at the DMA inlet, the monodisperse aerosol classified by the DMA

is then given by $n_1(Z_p)\Omega(Z_{p\text{DMA}}^*, Z_p)$, where $\Omega(Z_{p\text{DMA}}^*, Z_p)$ is the DMA transfer function and $Z_{p\text{DMA}}^*$ the centroid mobility corresponding to the DMA classifying voltage. Particle charging efficiency and penetration efficiencies within both the DMA and the plumbing system have been omitted above and are represented by an effective size distribution $n_1(Z_p)$. Using the FIMS transfer function, we can write the response of FIMS to the DMA classified aerosol as

$$\left(\frac{dN}{dZ_p^*}\right)_{\text{FIMS}} = \int_0^\infty n_1(Z_p)\Omega(Z_{p\text{DMA}}^*, Z_p)P(Z_p, Z_p^*, \sigma) dZ_p, \quad (4)$$

where Z_p^* is the instrument response mobility defined in Paper I, the FIMS response $(dN/dZ_p^*)_{\text{FIMS}}$ is described by the instrument response mobility distribution of the particles measured by the FIMS, and $P(Z_p, Z_p^*, \sigma)$ is the FIMS transfer function. Note that the transfer function is expressed as a function of the spread factor σ , since it will be treated as an independent variable in the subsequent analysis. It should also be pointed out that transfer function $P(Z_p, \tilde{Z}_p^*)$ given in Eq. (43) of Paper I is based on the normalized instrument response mobility \tilde{Z}_p^* . $P(Z_p, Z_p^*, \sigma)$ in Eq. (4) is based on Z_p^* , and can be related to $P(Z_p, \tilde{Z}_p^*)$ using the following equation:

$$P(Z_p, Z_p^*, \sigma) = P(Z_p, \tilde{Z}_p^*) \frac{d\tilde{Z}_p^*}{dZ_p^*} = \frac{1}{Z_p} P(Z_p, \tilde{Z}_p^*). \quad (5)$$

Inserting Eqs. (5) and (43) from Paper I into Eq. (4) above, we have

$$\begin{aligned} \left(\frac{dN}{dZ_p^*}\right)_{\text{FIMS}} &= \int_0^\infty \left(n_1(Z_p)\Omega(Z_{p\text{DMA}}^*, Z_p) \frac{1}{2\beta Z_{p\text{max}}^*} \right. \\ &\quad \times \left. \left\{ \text{erf}\left(\frac{\tilde{Z}_p^* - 1 + (1/2)\beta\tilde{Z}_{p\text{max}}^*}{\sigma}\right) - \text{erf}\left(\frac{\tilde{Z}_p^* - 1 - (1/2)\beta\tilde{Z}_{p\text{max}}^*}{\sigma}\right) \right\} \right) dZ_p. \end{aligned} \quad (6)$$

In the above equation, the polydisperse aerosol distribution $n_1(Z_p)$ was measured using the DMA and CPC. The DMA transfer function $\Omega(Z_{p\text{DMA}}^*, Z_p)$ was evaluated using the analytical expression given by Stolzenburg (1988). The DMA transfer function derived by Stolzenburg (1988) has been shown to reproduce experimentally determined mobility resolutions (Stolzenburg, 1988) at an aerosol to sheath flow ratio of 10, which is the same flow rate ratio used in our experiments. Given $n_1(Z_p)$, $\Omega(Z_{p\text{DMA}}^*, Z_p)$, and the FIMS dimensions and operating parameters, one can calculate the response of FIMS to the DMA classified aerosol using Eq. (6).

Fig. 7 shows an example of the response mobility distribution obtained from FIMS measurements (shown by symbols) for 90 nm classified particles at $Q_t = 9.7$ lpm. Also plotted on the same figure are predicted response distributions of the FIMS using Eq. (6) for various scenarios: (i) distribution with the spread factor (σ) computed using Eq. (44) from Paper I, (ii) distribution with two arbitrary values of σ —0.05 and 0.07, and (iii) the best fit to the experimental data. The best non-linear least squares fit to the experimental data yielded a spread factor $\sigma = 0.029$, which is slightly larger than 0.017 calculated using Eq. (44) in Paper I. Fig. 7 shows that there is a little difference among the FIMS response distributions predicted using σ of 0.017, 0.029, and 0.05; all predicted curves agree well with the experiment data. The low values of σ indicate that the effect of particle diffusion on the FIMS transfer function is small, and the spread of the transfer function is mainly controlled by the uncertainty in flow streamlines along which particle are introduced. As a result, the FIMS transfer function is insensitive to σ at low values of σ , which leads to the weak dependence of FIMS response to σ evident in Fig. 7.

Experimental spread factors were also calculated for a range of particle diameters in Units 2 and 3 by fitting Eq. (6) to the measured response mobility distributions, and are reported in Table 2. Fig. 8 shows the best fits to the experimental data for four particle sizes. Fitting was performed over the data for which the concentration exceeded 4% of the peak value. Table 2 also shows theoretical spread factor (σ) values calculated using Eq. (44) of Paper I. At Q_t of 9.7 lpm, the experimental spread factor agrees well with the theoretical prediction for small particles (i.e., particle with large σ)

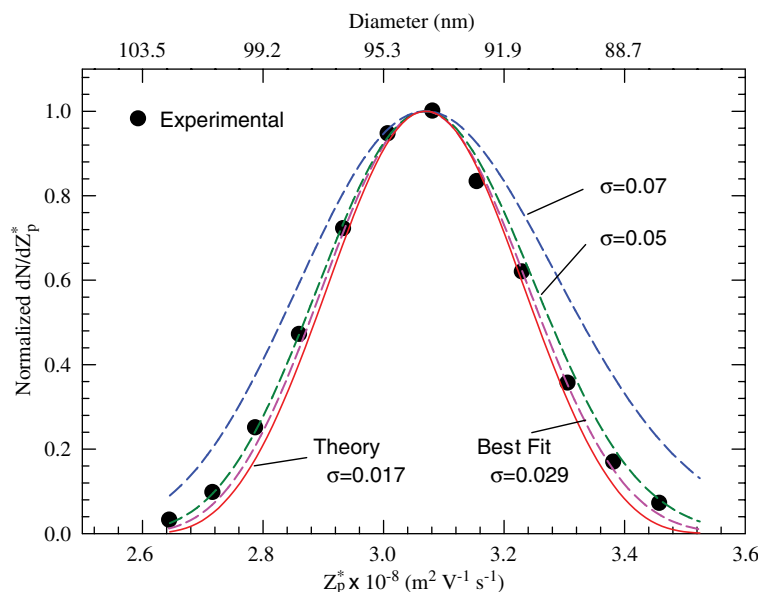


Fig. 7. Measured (symbol) and theoretically predicted (lines) mobility response distributions of FIMS to the DMA classified monodisperse aerosol.

Table 2

Experimentally derived and predicted spread factor (σ) at two flow rates for Units 2 and 3

DMA centroid diameter (nm)		Spread factor, σ			
		$Q_t = 9.7$ lpm		$Q_t = 11.85$ lpm	
		Calculated ^b	Experimental ^a	Calculated ^b	Experimental ^a
Unit 2	22	0.044	0.034 (10.5)	0.040	0.182 (1.5)
	24	0.047	0.042 (8.5)	0.042	0.199 (3.4)
Unit 3	50	0.010	0.051 (7.7)	—	—
	55	0.011	0.044 (9.3)	—	—
	60	0.012	0.035 (21.1)	0.011	0.041 (6.0)
	90	0.015	0.035 (12.2)	0.014	0.058 (1.9)
	120	0.018	0.036 (11.1)	0.016	0.062 (6.8)
	150	0.020	0.037 (20.6)	0.018	0.056 (13.6)
	170	0.021	0.043 (5.1)	0.019	0.061 (8.8)

^a Averaged over ten runs; numbers in parenthesis indicate % relative standard deviation.

^b Calculated using Eq. (44) in Paper I.

in Unit 2. However, for larger particles (i.e. particles with lower σ) in Unit 3, the experimentally derived σ is higher than the theoretically predicted value. This trend of better agreement between the experimental and predicted values of the spread factor for smaller particles is consistent with the earlier observations reported by Zhang and Flagan (1996) in their study on radial DMA. Zhang and Flagan (1996) also found that the experimentally determined spread factors for the radial DMA were higher than the corresponding theoretical values at lower values of σ .

For particles with low spread factors, the observed discrepancy in this study could be partially due to the large uncertainty associated with the experimentally derived values of σ . As discussed earlier, the FIMS transfer function is a weak function of σ at low σ values due to the small role of particle diffusion. As a result, the FIMS response is insensitive to σ , and there could be substantial uncertainty associated with σ derived by fitting Eq. (6) to the measured response distribution. This is further supported by the good agreement between the FIMS resolution, calculated using the

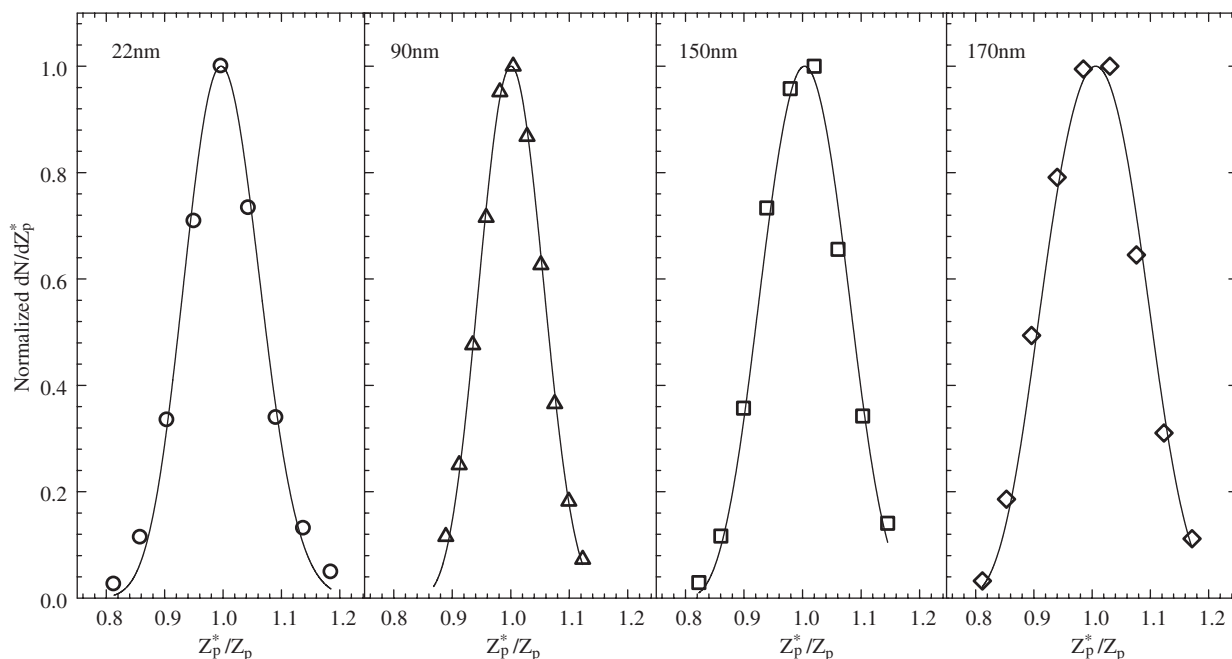


Fig. 8. Least-square fits to the response of the FIMS. The spread factor (σ) was used as an adjustable parameter.

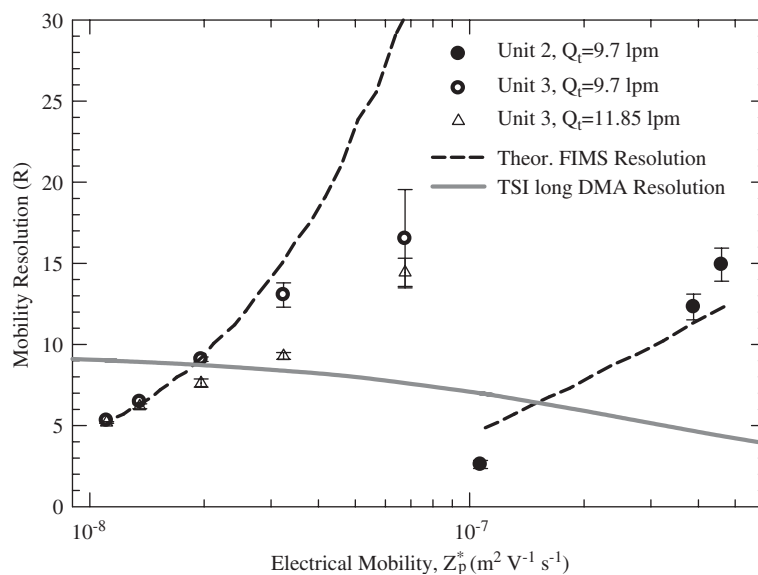


Fig. 9. Comparison of the FIMS resolution calculated using the experiment derived σ to theoretical resolution. Also shown is the theoretical resolution of the cylindrical DMA (TSI Inc. model 3081) with $\beta = 0.1$ for the corresponding mobility range.

theoretically predicted and experimentally derived spread factors as shown in Fig. 9, despite the substantial difference in predicted and derived σ at low values.

For particles measured by Unit 3, slightly larger discrepancies between predicted and derived values of σ were observed for small particles, and could be partially due to the non-uniform electric field at the exit of the separator. As the non-uniform electrical field is the strongest near the end of the HV electrode (right electrode in Fig. 1), it could be

expected that this non-uniform field has greater influence on the transport of smaller particles, whose trajectories are closer to the HV electrode.

As discussed in Paper I, a higher flow rate results in a lower particle residence time within the separator, and hence reduced diffusional spreading of the FIMS transfer function. However, Table 2 shows a reverse trend; as the total flow is increased from 9.7 to 11.85 lpm, higher values of experimentally derived σ were observed. This suggests that increasing flow rate enhances broadening of the FIMS transfer function. The higher experimental values of σ at $Q_t = 11.85$ lpm could be explained by the increased flow distortion at the aerosol entrance slit that possibly leads to the spreading of particles over a larger region than that predicted by the simplified transfer theory in Paper I. Higher flow rate could also enhance flow distortion at imperfect surfaces on the channel walls (e.g. joints between sections), resulting in higher experimental values of the spread factor.

The effect of particle diffusion on the FIMS transfer function can further be examined by the FIMS mobility resolution, defined in Paper I as $R = Z_p / \Delta Z_{\text{fwhh}}^*$, where ΔZ_{fwhh}^* is full width at half-height of the FIMS transfer function. The FIMS mobility resolution can be calculated using Eq. (43) of Paper I, given the spread factor σ .

Fig. 9 shows the FIMS mobility resolution R calculated using experimentally derived σ (represented by symbols) for Units 2 and 3 at $Q_t = 9.7$ lpm, and for Unit 3 at $Q_t = 11.85$ lpm. Also shown by dotted lines are theoretical resolution of the two FIMS units, and the mobility resolution of a TSI cylindrical DMA (Model 3081) at $\beta_{\text{DMA}} = 0.1$ (with aerosol and sheath flow rate of 1, and 10 lpm, respectively). For particles measured by Unit 2, the experimental resolution (i.e. resolution calculated using experimentally derived σ) agrees well with the theoretical resolution of FIMS. For Unit 3, the experimental resolution agrees with the theoretical resolution only at low particle mobilities (larger particle sizes); there is significant deviation from high theoretical resolution at larger particle mobilities (for particle diameters < 90 nm). This deviation from the theoretical resolution increases with increasing particle mobility in a given unit. At high theoretical resolution, the spread of the FIMS transfer function due to uncertainty from finite stream width of aerosol flow and particle diffusion is small. The additional spread in the transfer function due to non-idealities in flow or electrical fields (or from any other unknown factors) may become comparable and lead to significantly lower mobility resolution. In contrast, at low theoretical mobility resolutions, the additional spread due to non-idealities is unlikely to result in substantial reduction in already low mobility resolution. Previous studies of cylindrical DMA and radial DMA have shown similar deviation of resolution at high theoretically predicted resolution (Stolzenburg, 1988; Zhang & Flagan, 1996). Besides the non-ideal electric field at the separator exit, the observed deviation from the theoretical resolution could also be due to redistribution of particles over a wider region as a result of flow distortions induced by minor protrusions or mechanical imperfections along the channel walls, particularly at the flange joints between the various sections. In both units, the deviation from the theoretically predicted resolution is more pronounced at the higher flow rate (11.85 lpm), which may be attributed to enhanced flow distortions at imperfect surfaces.

The fluid mechanical disturbances at the aerosol entrance slit may also be of concern. The degradation in resolution of the cylindrical DMA and radial DMA has been partially attributed to flow disturbance in the aerosol entrance slit (Zhang & Flagan, 1996). Zhang and Flagan (1996) suggested that the larger degradation in Radial DMA resolution could possibly be attributed to higher shear produced by the tangential aerosol flow. The aerosol flow in the FIMS enters the main channel at an angle of 30° with respect to the direction of the sheath flow, possibly experiencing larger tangential shear. However, for particles measured by Unit 2 with mobility $3.9 \times 10^{-7} \text{ m}^2 \text{ V}^{-1} \text{ s}^{-1}$ (24 nm) and $4.6 \times 10^{-7} \text{ m}^2 \text{ V}^{-1} \text{ s}^{-1}$ (22 nm) that correspond to high theoretical spread factor, the above mechanisms do not seem to affect the FIMS mobility resolution (Fig. 9). Zhang and Flagan (1996) also reported better agreements between experimental and theoretical resolutions for particles with high σ in radial DMA. The improvement of instrument resolution and the effects of non-idealities in flow and electric fields will be a subject of future studies.

As noted in Paper I, opposite trends in resolution with increasing particle mobility for FIMS and conventional DMA are also evident in Fig. 9. The spread in the FIMS response mobility resulting from high diffusivity of small particles is offset by the increasing particle mobility; as a result, the resolution of smaller particles is higher compared to that of larger particles in a FIMS unit.

4. Conclusions

A Fast Integrated Mobility Spectrometer (FIMS) has been developed for high time-resolution measurements of particle size distributions. The performance of FIMS has been characterized using monodisperse, DMA classified

aerosols in the size range from 15 to 170 nm. Particle sizes measured by FIMS agree well with the DMA centroid diameters, indicating that FIMS is capable of measuring particle size with high accuracy. The counting efficiency of FIMS is nearly 100% for particles larger than 20 nm, and exceeds that of a CPC (TSI model 3760A) for particles smaller than 15 nm. The influence of particle diffusion on the FIMS mobility resolution has also been investigated. In a single FIMS unit, experimentally determined mobility resolution agreed well with the theoretical values at low particle mobilities that correspond to low theoretical resolutions. For particles with high mobility corresponding to high theoretical resolution, the experimental resolution was lower than the theoretical predictions. The degradation in resolution was partially attributed to the non-idealities in flow and electric fields in the FIMS. The measurement resolution of FIMS is found to be at the least comparable, and mostly superior, to that of conventional DMAs under typical operating conditions.

Acknowledgements

This work was supported by the Office of Biological and Environmental Research, Department of Energy, under contract DE-AC02-98CH10866, the Office of Global Programs of National Oceanic and Atmospheric Administration under contract NRMT0000-5-203, and the Laboratory Directed Research and Development program at Brookhaven National Laboratory. Stimulating discussions with Drs. Peter Takacs, Peter Daum, and Stephen Springston are gratefully acknowledged. Jian Wang also acknowledges partial support from the Goldhaber Distinguished Fellowship from Brookhaven Science Associates.

References

- Agarwal, J. K., & Sem, G. J. (1978). Generating submicron monodisperse aerosols for instrument calibration. *TSI Quarterly*, *IV*(2), 3–8.
- Kousaka, Y., Okuyama, K., Adachi, M., & Mimura, T. (1986). Effect of Brownian diffusion on electrical classification of ultrafine aerosol particles in differential mobility analyzer. *Journal of Chemical Engineering Japan*, *19*, 401–407.
- Rader, D. J., & McMurry, P. H. (1986). Application of the tandem differential mobility analyzer to studies of droplet growth or evaporation. *Journal of Aerosol Science*, *17*(5), 771–787.
- Stolzenburg, M., 1988. *An ultrafine aerosol size distribution measuring system*. Ph.D. Thesis. University of Minnesota.
- Zhang, S.-H., & Flagan, R. C. (1996). Resolution of the radial differential mobility analyzer for ultrafine particles. *Journal of Aerosol Science*, *27*(8), 1179–1200.